Wrinkling in shrink flanging by single point incremental forming

J.A. López-Fernández*, G. Centeno, C. Vallellano

Department of Mechanical and Manufacturing Engineering,
University of Seville, Camino de los Descubrimientos s/n 41092, Sevilla (Spain)
*Corresponding author, Telephone number: +34 954 48 13 60, email: jlopez85@us.es

Abstract:

Conventional flanging processes are commonly used in the automotive and aeronautical industry to provide stiffness or support for further assembly of thin-walled structures. Incremental flanging has emerged as a promising flexible and low-cost alternative to conventional processes for small batch production. This work presents a systematic experimental and numerical analysis of formability and failure within the forming limit diagram (FLD) of shrink flanges performed on AA2024-T3 sheet by single point incremental forming (SPIF). A series of tests varying the initial width, length and die radii of the flange are carried out under different process conditions, stablishing the practical process window for different flange radii, spindle speed and tool diameter. The results show two modes of failure for the larger flange radius, failure by wrinkling and failure by incipient wrinkling, and only failure by incipient wrinkling for the smaller die radius. The deformation mechanism of successful flanges and the wrinkling initiation are analysed obtaining strain points below the pure compression line ($\beta = -2$) in the FLD and pointing out that this limit does not provide a unique wrinkling limit curve (WLC) for this process. Finally, the stress evolutions of a set of flanges is analysed using an explicit finite element model. It is found that wrinkling in shrink flanging by SPIF occurs when the minor principal stress (compressive stress) reaches a certain critical level. Below this level, flanges are successfully formed. On that basis, a numerical methodology to predict the onset of wrinkling is proposed. This allows identifying the winkling limit as the minor principal stress at the edge of the flange that triggers the wrinkling process.

Keywords: Single point incremental forming (SPIF); shrink flanging; formability; wrinkling; numerical modelling; wrinkling prediction.

Acknowledgement

The authors acknowledge the Spanish Government for founding this work through the research projects DPI2015-64047-R and PGC2018-095508-B-I00.

1. Introduction

The flanging process is widely established in the automotive and aeronautical industry to provide stiffness or support for further assembly in sheet metal parts. This consists of bending, usually at 90º, the perimeter of the part along a given line. Regarding the curvature of the bending line, three elemental types of flanges can be distinguished, that is, straight, concave, or convex flange, respectively (see Fig. 1, left). In the first case, the material is locally bent with a given radius along a straight contour, remaining undeformed the rest of the flange. In the second, also referred to as stretch flange, the material is subjected to a combination of bending and stretching, being the ductile fracture the most likely mode of failure. In the last one, also named shrink flange, the material supports bending and compression. The expected mode of failure is the appearance of wrinkling caused by local buckling. Different combinations of these elemental flanges, such as reverse flanges, joggled flanges, and hole flanges are also common in industrial practice. Figure 1 (right) depicts typical aeronautical ribs showing several of these features.

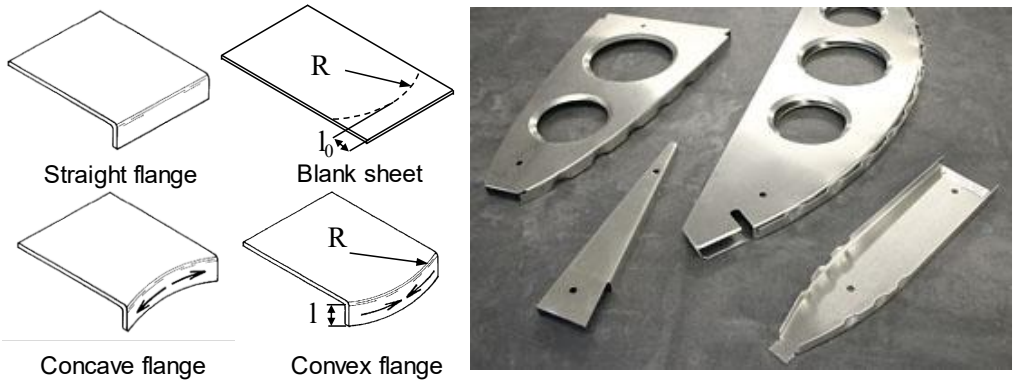

Figure 1. Basic type of flanges (left). Typical aeronautical ribs (right) [1].

Conventional flanging used in mass production, e.g. in the automotive industry, is mainly performed by press working or stamping, using punches and dies. Whereas, for medium or small batch production, as usual in the aeronautical industry, the use of rubber forming and fluid forming is more common. Understanding the geometric, material, and process parameters that limit the formability of the flange (i.e., *flangeability*) is of primary importance in industrial practice, and has received ongoing research effort for decades. The pioneering work by Dudra and Shah [2] on stretch flanging of 1008 AK steel sheets analysed the influence of flange radius and length. They pointed out that flanges with original length versus curvature radius l_0/R (see figure 1 (left)) above 0.725 developed splits or necks. Asnafi [3] performed an exhaustive experimental and numerical study of stretch and shrink flanging of AA2024-O and AA6061-O sheets by fluid forming, finding that failure appears for length-

to-radius ratio above 0.43 and 0.9 respectively (average)in stretch flanges, whereas for shrink flanging the conditions were much more demanding, obtaining length-to-radius ratios in the range 0.08 - 0.09 on average. The work by Livatyali et al. [4] pointed out that the l_0/R ratio must be below 0.05 for avoiding wrinkling in AKDQ and BH steel sheets respectively. Similar limits were recently obtained by Chen et al. [5] for aluminium alloys: $l_0/R < 0.057$ for 2024-O, $l_0/R < 0.04$ for AA7075-O, and $l_0/R < 0.02$ for AA2024-T3. For large curvature radii (ranging from 500 to 2000mm), Wang et al. [6] found critical l_0/R ratios ranging from 0.016 to 0.006 forAA6111-T4 and AA6022-T4 sheets respectively. The low values of limiting l_0/R ratio in shrink flanging are often compensated using methods that control the height and shape of the wrinkles [7] or applying other forming technologies that increase the material flangeability such as incremental forming.

In the last decades, incremental sheet forming technologies have emerged and developed as promising flexible forming processes, especially for small batch production, prototypes, and highly customized parts. Incremental sheet forming (ISF) processes pursue the local and progressive deformation of the metal sheet until its final shape using a CNC guided forming tool that follows a pre-established trajectory. The use of dedicated and expensive dies as common in conventional processes is not needed. Emmens et al. [8] published an overview of SPIF technology, focusing on the origin and evolution of the different variants of ISF. The simplest version of ISF processes is single-point incremental forming (SPIF), in which a peripherally clamped blank is formed using a hemispherical tool. A very complete review describing many technological aspects, advantages, and applications of ISF was published by Jeswiet et al. [9]. In addition to flexibility, cost savings and the reduction of forming forces, the most relevant advantage of the SPIF compared with conventional forming is the apparent improvement of material formability. The factors affecting this formability enhancement are a matter of discussion today. The different stabilizing mechanisms involved in ISF were reviewed by Emmens and Van den Boogaard [10], and the influence of the main process parameters were discussed by Gatea et al. [11].

SPIF and, by extension, ISF, have been successfully applied to produce flanges in holes in sheet metal parts using different strategies. The work of Cui and Gao [12] applied different multi-stage SPIF strategies to control the thinning of the material in circular hole flanging (stretch flanging). Several multi-stage strategies have been also used efficiently by Movahedinia et al. [13] to perform a flaring process to thin-walled tubes, showing a significant increase in the maximum semi-apex angle. In an effort for reducing the time production per part and increasing formability, different strategies and tools were used. Allwood and Shouler [14] introduced a variant of hole-flanging by ISF using non

hemispherical tools called paddle forming, which increase the hole expansion ratio achieved by hole flanging as recently showed by Besong et al. [15]. Chen et al. [16] and Wen et al. [17] analysed different factors and proposed new tool geometries respectively to increase formability in hole flanging by SPIF respectively. Martins and co-workers analysed in detail the formability of circular flanges produced by multi-stage forward SPIF [18,19]. Thus, Centeno et al. [18] used the conventional forming limit curve (FLC) and the fracture forming limit (FFL) to predict the failure in conical and cylindrical hole-flanges by SPIF. Likewise, Cristino et al. [19] suggested the use of critical ductile damage and critical fracture toughness values to establish the formability limits. Martinez-Donaire et al. [20] and more recently Sayyedi et al. [21] evaluated the formability from a different approach based on the damage accumulation due to the growth of voids in the material. Borrego et al. [22] and Morales-Palma et al. [23] explored formability in a less time-consuming but more demanding strategies, such as hole flanging by single-stage and two-stage SPIF respectively.

The amount of research papers on open flanging by ISF in the literature is scarce compared to hole-flanging. Voswinckle et al. [24, 25] provided an exhaustive analysis of the influence of geometric and process parameters on the formability and geometric accuracy for open stretch and shrink flanging by single and multi-stage SPIF of cold-rolled mild steel grade DC04. They did not observe any benefit of complex strategies with respect to the single-stage strategy, being the latter also preferable in terms of surface quality and roughness of the flange. The maximum l_0/R ratio obtained was 0.2 and 1 for die radii of 100 and 20 mm, respectively, for both types of flanges. This represented a remarkable gain in formability 10 times higher for shrink flanges with respect to convectional flanging. Zhang et al. [26] conducted an experimental and numerical study of the deformation mechanics and failure of stretch and shrink flanges in holes produced by double-sided incremental forming in AA5754-O sheets. Again, incremental flanging showed a gain of formability in both type of flanges, but more notable in shrink flanges, reaching a l_0/R ration around 0.316, which was about 10 times the expected value in a conventional process. Recently, the work of Lopez-Fernández et al. [27] has studied the mechanisms of deformation and failure and the influence of the parameters of the processes to manufacture open stretch flanges of AA2024-T3 using single-stage SPIF, highlighting the capability of the incremental process to successfully form low-ductility alloys.

The formability limits by necking and fracture are well established in conventional sheet metal forming [28], providing the forming limit diagram (FLD) an excellent framework for analyzing the flangeability in stretch flanges. However, this is not as straightforward in the case of shrink flanges. The existence of a universal wrinkling limit curve (WLC) in the principal strain diagram, in the same

way as the FLC for necking and the FFL for the tensile fracture, has been an appealing idea since decades. Havranek [29] was pioneer in suggesting a WLC in the second quadrant of the principal strain space for conical cups. Szacinski and Thompson [30] analysed the pressing of sink-bowls of annealed 301 austenitic stainless-steel 0.9 mm thick. No discernible distinction could be found between the strains associated with wrinkled and unwrinkled areas in their tests, noting that the onset of the wrinkling was determined not only by the magnitude of the total deformation (as is roughly the case in necking or fracture), but also by the geometry of the specimen and the test conditions. They concluded that a wrinkling limit curve cannot be obtained in a manner similar to that of commonly used FLC.

Narayanasamy and Sowerby [31] carried out conical cup drawing tests with different punches, lubricant conditions and two materials (stainless steel 304 grade and dual phase steel type A). The found that the slope of the curve $d\varepsilon_1/d\varepsilon_2$ changed suddenly when a wrinkle develops on the blank and remained constant, with a value depending on the test, when there was no wrinkling. The critical ratio $d\varepsilon_1/d\varepsilon_2$ at the onset of wrinkling was dependent on the material, having a value of -0.65 for the stainless-steel 304 (corresponding to $\beta = -1.54$), and -0.32 for the dual-phase steel (corresponding to $\beta = -3.12$). They suggested the existence of a WLC in the second quadrant of the principal strain space but depending on the material and the test conditions.

Wang et al. [6] developed analytical solutions for the onset of wrinkling in the shrink flanging of an elastic-plastic sheet using the energy method. Under the appropriate boundary conditions, they provided the critical stress condition for wrinkling in terms of geometric dimensions and material properties. They found that the critical flange length depends largely on the die radius, the sheet thickness, and material hardening exponent, and is almost unsensitive to the sheet anisotropy.

More recently, Magrinho et al. [32] determined the critical wrinkling condition at the edge of the flanges of deep-drawing cups performed without blank holder by analyzing rectangular specimens of different thickness. They provided the WLC in the FLD for this geometry, showing an initial straight part, coinciding with the pure compression line (i.e. $\beta = -2$), followed by a curved shape towards smaller slopes. The last point in the straight part corresponded to the last admissible pair of critical strains prior to wrinkling.

The number of studies addressing the onset of wrinkling in the case of incremental processes is very limited. Most of the work is focused on spinning and related processes. To this regard, Hartel and

Awiszus [33] conducted a technological and phenomenological research that showed some benefits of using a convex forming tool instead of a cylindrical one, such as the reduction of wrinkling and a higher thinning of the sheet. Chen et al. [34] presented a theoretical model for the prediction of wrinkling in spinning that is based on the critical value in the circumferential stress achieved in the flange. Despite the number of works focused on the study of the wrinkling appearance in conventional and, to a lesser extent, in incremental processes, there is no consensus on the existence of a universal WLC within the FLD, nor a unified methodology to predict the appearance of wrinkles in incremental processes. This is mainly due to the number of factors that influence the local buckling process of the sheet, such as material properties, geometric parameters of the part, process conditions, etc.

The current work presents for the first time a systematic analysis of the deformation and failure mechanisms of shrink flanging by single-stage SPIF in AA2024-T3 sheet. The high strength and good corrosion resistance of the T3 temper makes this alloy widely used in aircraft parts. However, its low ductility requires that complex parts be formed after an initial solution heat treatment (W temper) to increase ductility, subsequently reaching its original strength by natural aging (T4 temper), incurring substantial extra cost. It is clearly shown that the incremental deformation allows to produce shrink flanges directly in T3 temper, improving the flange formability, as recently also pointed out by the authors in stretch flanges [27].

For this study, an experimental campaign is designed to test the flangeability and geometric accuracy under different shrink flange geometries, such as several initial widths, lengths, and die radii, under two spindle speeds and two tool diameters. The evolution of the strains along the flanges and the modes of failure are analysed in the FLD using the Argus® optical strain analysis system. It has been corroborated that the pure compression line ($\beta = -2$) does not define a distinctive WLC for this incremental flanging process. Finally, a FE-based methodology is proposed to predict the appearance of wrinkles in incremental shrink flanging by SPIF.

2. Material characterization

This section presents the experimental methodology used to determine the mechanical properties in terms of elastic-plastic behaviour, mechanical anisotropy and formability limits, of the 1.2 mm thickness aluminium alloy 2024-T3.

Table 1. Mechanical properties including anisotropy coefficients along rolling directions

Direction	σ_Y *(MPa)*	σ_{UTS} *(MPa)*	*E (GPa)*	ν	$\bar{r}_\theta$

0°	336	445	69.4	0.33	0.76
45°	306	427	67.1	0.33	0.95
90°	319	443	68.2	0.33	0.54

2.1. *Tensile properties*

Tensile tests were carried out along the three characteristic directions of the sheet, the rolling direction (RD or 0°), the transverse direction (90°) and the diagonal direction (45°). These tests were performed in a universal INSTRON™ 1196 testing machine following the specifications of the standard ASTM E8/E8M – 09 [35]. Figure 2a depicts the resulting true stress-strain curves for the three different directions obtained using an axial extensometer Epsilon® model 3542. The extensometer was removed just before fracture to prevent damage. The mathematical expression of a Swift's law fitted at 0° is also given. Tensile properties are shown in Table 1, including the yield stress σ_Y, the ultimate tensile strength σ_{UTS} and the modulus of elasticity E along the mentioned directions. As a first approximation, the Poisson ratio ν is assumed to be 0.33 along each direction. The Lankford coefficients $r_{0°}$, $r_{45°}$ and $r_{90°}$ were obtained according to the standard ASTM E 517 – 00 [36] by unloading at three different strain levels, equispaced along the plastic regime. The average values $\bar{\boldsymbol{r}}_{\boldsymbol{\theta}}$ for the three directions are given in Table 1.

2.2. Forming limit diagram (FLD)

The formability limits were obtained via Nakazima tests in a universal testing machine Erichsen® model 142-20 using a hemispherical punch of 100 mm diameter (see Figure 3a). They were performed according to the standard ISO 12004-2:2008 [37]. The punch speed was set to 1 mm/s and a tribological layer of Vaseline - PTFE – Vaseline was placed between the punch and the specimens to minimize friction. Five specimen geometries reproducing strain states ranging from uniaxial to equibiaxial strain were tested to obtain the forming limits (see the schema and a picture of the tested specimens in Figure 2b. Each geometry was tested at least three times in order to provide statistical meaning to the results.

The strain evolutions were obtained using the 3D Digital Image Correlation (DIC) system Aramis® version 6.3 with 1.3 megapixel cameras. The frame rate was set to 12 images per second using square facets of 13 x 13 pixels with 2 pixels of overlapping. The experimental strain paths of the different Nakazima specimens are depicted in Figure 2b.

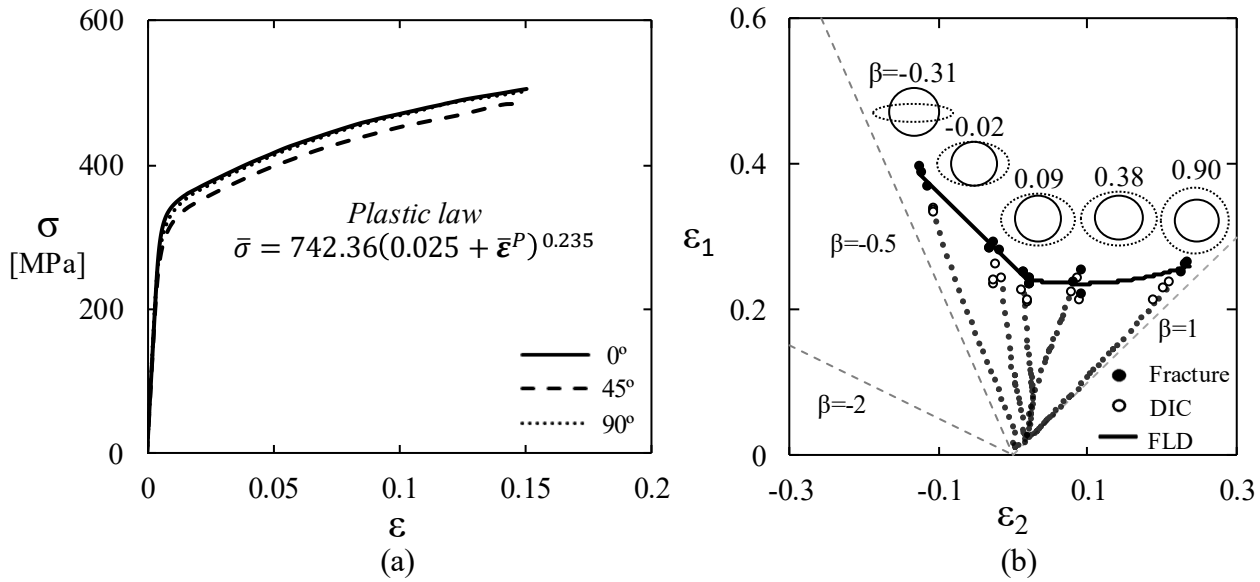

Figure 2. (a) Stress strain curves for different directions respect to the rolling direction. (b) Forming limit diagram of AA2024-T3 represented by the FFL obtained using five strain paths along with the strain ratio β corresponding to the different testing specimens.

The temporal methodology proposed by Martinez-Donaire et al. [38] and the standard ISO 12004-2:2008 [37] were used to identify the onset of necking. However, none of them evidenced the appearance of necking prior to fracture. Such absence of local necking agrees with the studies carried out by Vallellano et al. [39] and Centeno et al. [40].

The common procedure to obtain the FFL for materials with necking, see, for instance, Silva et al. [41], Centeno et al. [18] and Borrego et al. [22], is based on the methodology proposed by Silva et al. [42]. This method assumes that the strain evolution in Nakazima tests exhibits a kink towards vertical direction (in the FLD) after the neck initiation, which, as detailed by Skjoedt et al. [43], allows obtaining the major strain at fracture by measuring the thickness reduction at fracture. However, because this material does not present necking, this method cannot be applied directly, and it is modified as follows.

As can be seen in Fig. 2b, the experimental strain paths recorded with DIC maintain an almost constant strain ratio $\beta = \varepsilon_2/\varepsilon_1$ until close to fracture. It is assumed that this strain ratio also continues from the last image recorded using DIC to the onset of fracture, providing a relationship between the major and minor strains at fracture, ε_{1f} and ε_{2f} respectively (Eq.1). On the other hand, the thickness strain at fracture ε_{3f} is obtained experimentally by measuring the sheet thickness at fracture t_f

through the equation $\varepsilon_{3f} = \ln(t_f/t_0)$, where t_0 is the initial thickness of the sheet. In this work, t_f was estimated as the average thickness at the crack lips in both sides of specimen at the point of maximum thickness reduction recorded by the DIC system. Each part of the sample was polished perpendicular to the crack and the thickness of the crack lip was measured using a NICON® SMZ800 microscope and the software KAPPA® Image Base Metreo version 2.7.2. Finally, assuming volume constancy at fracture (Eq. 2), the major and minor strains, ε_{1f} and ε_{2f}, at fracture are obtained by applying Eq. 3. The estimated principal strain at fracture for the different Nakazima specimens and the resulting FFL are presented in Figure 2b.

$$\varepsilon_{2f}/\varepsilon_{1f} \approx \beta \tag{1}$$

$$\varepsilon_{1f} + \varepsilon_{2f} + \varepsilon_{3f} = 0 \tag{2}$$

$$\varepsilon_{1f} \approx \varepsilon_{3f}/(1+\beta) \quad \therefore \quad \varepsilon_{2f} \approx \varepsilon_{3f}\,\beta/(1+\beta) \tag{3}$$

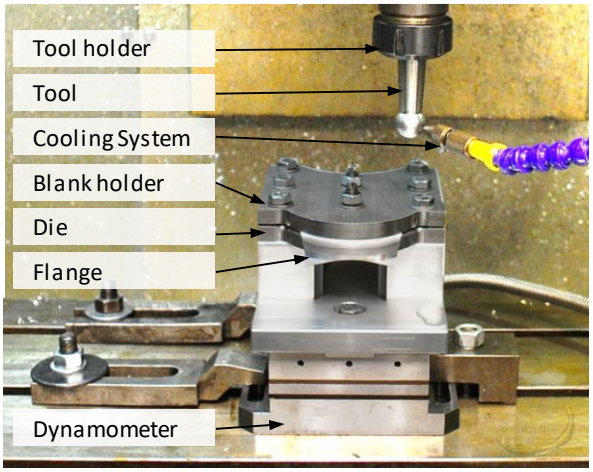

(a)

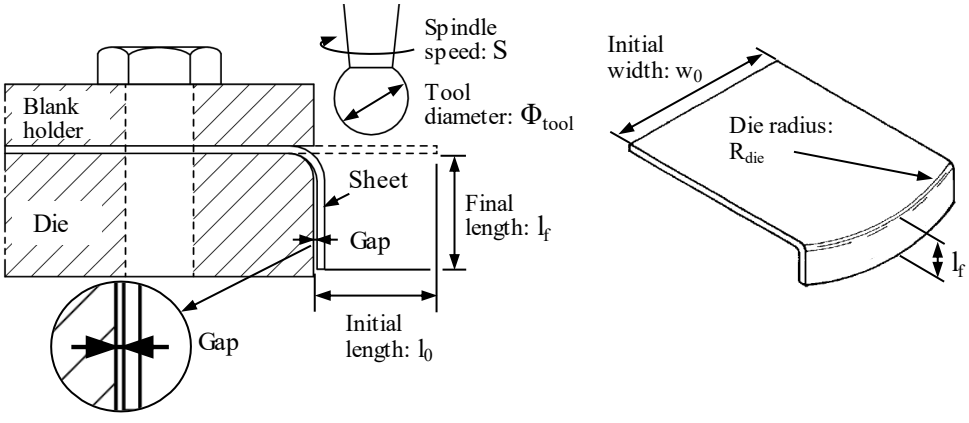

(b)

Figure 3. (a) Experimental setup for the flanging experiments corresponding to 45 mm of die radius with the convex flange. (b) Schematic representation of the elements involved in the flanging process by SPIF.

3. Shrink-flanging tests

The shrink flanges were performed using an EMCO VMC200 3-axis CNC milling machine. Figure 3a shows the different elements of the experimental set-up, that is, the forming die and sheet holder for a given convex radius. The bending radius in the forming die was 3 mm.

The SPIF operation was carried out in a single stage using hemispherical tools of different diameters. The tool path describes a series of alternating horizontal passes in circular arc with a constant step down (Δ_z) at the end of each pass. To avoid shearing of the sheet, an initial gap between the forming die and the forming tool of 1.4 mm was set. Therefore, assuming a nominal sheet thickness of 1.2mm, the functional gap between the forming die and the flange is around 0.2mm, as shown in Figure 3b. Additionally, the tool is forced to remain always in contact with the flange, particularly at the end of each arc.

Table 2. Process parameters analysed in the flanging tests

R_{die} (mm)	w_0 (mm)	l_0 (mm)	S (rpm)	ϕ_{tool} (mm)	Δ_z (mm)
45	36/ 45 / 54 / 63 / 72	10 / 15 / 20 / 25	20 / 1000	12 / 20	0.4
20	20 / 24 / 28 / 32 / 36				

A series of shrink flanges with different die radii (R_{die}), width (w_0) and length (l_0) were tested. Two die radii of 45 mm and 20 mm, representatives of small flanges in the industrial practice, were selected. The effect of different tool diameters (ϕ_{tool}) and spindle speeds (S) in the forming process was analysed. Table 2 summarizes the overall plan of experiments and the different parameters studied.

The feed rate was set constant to 1000 mm/min, and the tool rotation was set to either 20 rpm or 1000 rpm depending on the experiment. With the aim of minimizing the friction between the tool and the flange, Castrol Iloform TDN 81 was continuously spread over the tool using an air-oil mixing device that also had a cooling effect. The duration of the test varied depending on the die radius, width, and length of the flange, being ranged from 3 minutes to 20 minutes.

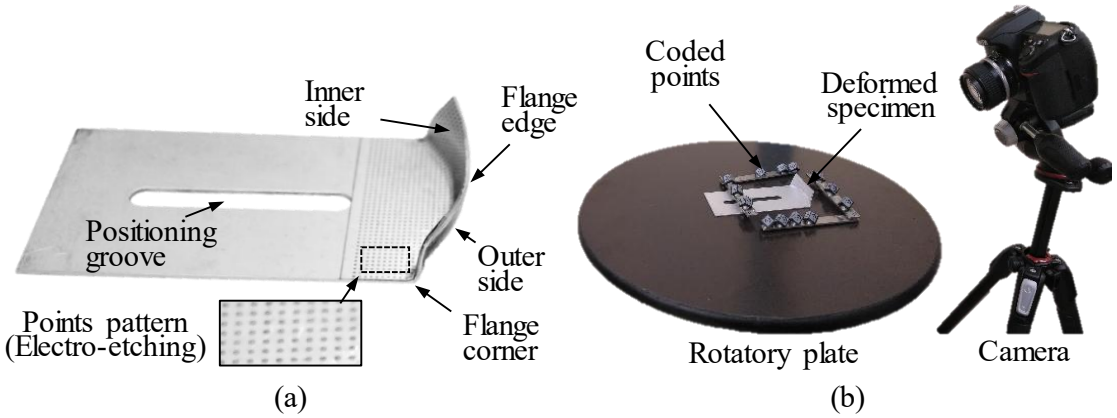

Figure 4. (a) Description of the different parts of the flange. (b) Elements of the CGA system Argus®.

The aluminium sheet was cut into rectangles and polished to remove imperfections that might nucleate early cracks during the flanging process. Then, the specimens were electro-etched obtaining the points pattern shown in figure 4a used to perform the strain measurement. The circular grid was positioned towards the non-contact surface of the specimen, otherwise contact with the forming tool would erase the pattern.

After the experiments, the specimens were analysed using the circle grid analysis (CGA) commercial system Argus®, obtaining the principal strains distribution of the non-contact surfaces of the blanks. The elements of the Argus® system (camera, coded points and positioning of the deformed specimen) are shown in Figure 4b. It should be noticed that this system needs of four grid points to interpolate the strains in between. Consequently, the strains at the very edge of the flange cannot be measured. For the flanges analysed, the typical distance from the last point measured by Argus® to the flange tip was approximately 0.5 mm.

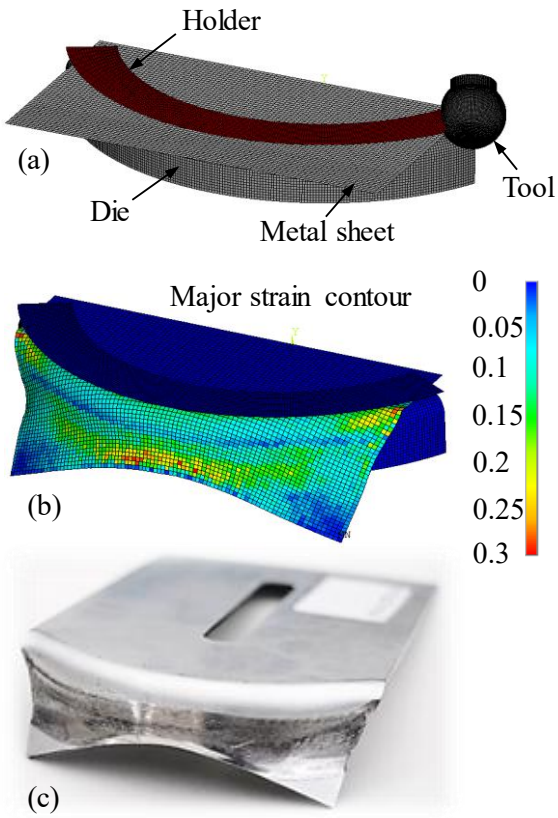

Figure 5. Finite Elements model: (a) undeformed mesh and (b) major strain distribution on the deformed flange and (c) the corresponding flange obtained from experiments.

4. Numerical modelling

A numerical model of the incremental shrink flanging process was used to analyse the stress/strain evolution in the flange and to perform the prediction of wrinkling described in section 6. To this purpose, a Finite Element (FE) model based on an explicit dynamic integration scheme was developed using the commercial software Ansys LS-Dyna®.

The simplified geometry of the model (blank holder, forming die, forming tool and undeformed specimen) is shown in Figure 5. The specimens were meshed using the 4-nodes SHELL163 element from the Ansys LS-Dyna®. The element formulation was Berlytschko-Tsay with stiffness hourglass control. An hourglass control coefficient of 0.1 was set according to the Ansys User's Guide recommendations. To select the element size, a sensitivity analysis was performed by reducing the characteristic element length from 1.5 to 0.2mm. It was concluded that sizes below 0.5 mm did not show a significant improvement in the results. Consequently, regular and uniform meshes of 0.5 mm element size were used to model the sheet specimens. The die, the blank holder and the forming tool were considered as rigid bodies.

The anisotropic yield criterion proposed by Barlat and Lian [44] for the modelling of the sheet under plane stress conditions was selected. The yield function is shown in Eq. (4) and (5)

$$f(\sigma) = a|k_1 + k_2|^m + a|k_1 - k_2|^m + c|2k_2|^m = 2\bar{\sigma}^m \tag{4}$$

$$k_1 = \frac{\sigma_{xx}+h\sigma_{yy}}{2} \quad \therefore \quad k_2 = \sqrt{\frac{\sigma_{xx}+h\sigma_{yy}}{2} + p^2\sigma_{xy}^2} \tag{5}$$

where $\bar{\sigma}$ is the yield stress and the parameters m, a, c, h and p are material constants. The exponent m is set 8 as suggested for FCC materials such as the aluminium alloys [45]. The constants a, c and h are given by

$$a = 2 - 2\sqrt{\frac{r_0 r_{90}}{(1+r_0)(1+r_{90})}} \quad \therefore \quad c = 2 - a \quad \therefore \quad h = \sqrt{\frac{r_0(1+r_{90})}{(1+r_0)r_{90}}} \tag{6}$$

and p implicitly obtained by solving the Eq. (7),

$$r_{45} = \frac{2\, m\, \bar{\sigma}^m}{\left(\frac{\partial f}{\partial \sigma_{xx}} + \frac{\partial f}{\partial \sigma_{yy}}\right)\sigma_{45}} - 1 \tag{7}$$

where r_0, r_{45} and r_{90} are the Lankford coefficients, and σ_{45} is the yield stress of 45º to the rolling direction given in Table 1. The yield stress $\bar{\sigma}$ is obtained by fitting a Swift-type law to the stress-strain curve at rolling direction (Fig. 2a). An isotropic hardening behaviour was assumed. A more detailed assessment of the Barlat-Lian yield criterion for the AA2024-T3 sheet used in the tests can be found in [27].

In ISF, the bending effects induced by the tools are of primary importance in understanding the sheet behaviour. The shell163 elements include bending capabilities and allow to define multiple integration points through the thickness. Five integration points were defined equally weighted and regularly spaced through the thickness of the sheet. This allows extracting the local variables (strains, stresses, etc.) in the layer of interest. In particular, in terms of strains, the most requested layer in the sheet during the forming process is the one that is opposite to the contact with the tool, hereafter named the outer surface. These numerical strains were compared with their experimental counterparts to validate the numerical model (see Section 6.1).

Modeling of clamping and contact conditions is also critical; see, for instance, Benedetti et al. [46]. As shown in Figure 3a, in the experimental set up, the sheet is fixed using a screwed blankholder. Before the forming step, a clamping step was introduced that simulates the positioning of the specimen where the blankholder moves vertically around 0.1 mm to apply the holding pressure to the sheet. This fairly well reproduces the experimental observation.

A master-slave surface-to-surface contact formulation with the Coulomb friction model was assumed between the sheet and the tool and dies. The friction coefficient was set to $\mu = 0.01$. This value was adjusted following an iterative procedure carried out in a previous work on incremental stretch flanges with identical experimental set up [27]. Briefly, an initial value of 0.05 was assumed, as suggested in the literature for regular lubrication [47], and it was progressively varied until reach the best concordance between the numerical and experimental results in terms of strains in the flange and tool force. Notice that a friction coefficient well below the 0.05 is quite consistent with the use of a continuous and local lubrication system, such as the one used.

Finally, to reduce the computational time, both a mass scaling factor of 5 and a time scaling factor of 1000 were employed. Depending on the initial length and width of the flange to test, the simulation time took from one to three hours in a workstation with an Intel® Xeon® CPU E3-1230 v6 (3.50 GHz) processor.

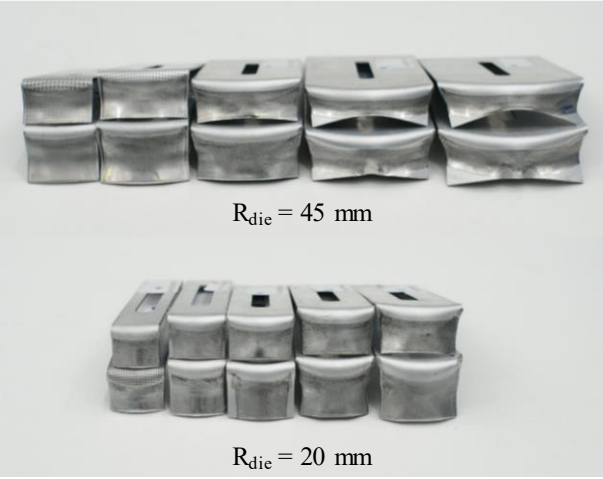

Figure 6. Resulting flanges for a selected case of process parameters ($\phi_{tool} = 12\ mm$ and $S = 20\ mm$) and die radii of 45 mm (above) and 20 mm (below), respectively.

5. Experimental results. Process window

This section aims to present the results obtained in the experimental campaign of shrink flanges by SPIF, including (i) a classification of their principal modes of failure and (ii) the assessment of the

influence of the main process parameters in their formality, establishing the practical process windows.

The flange series of different initial widths (w_0) and lengths (l_0) described in section 3 were tested. Figure 6 shows different examples of manufactured flanges of $R_{die} = 45$ mm and $R_{die} = 20$ mm. In tables 3 and 4 the flanges are classified attending to the defect observed after the SPIF operation. Four sub-tables are presented which corresponds to the combination of $\phi_{tool} = 20$ mm, $\phi_{tool} = 12\ mm$, $S = 20$ rpm and $S = 1000$ rpm respectively. To provide statistical meaning, at least two replicates were performed for each experiment.

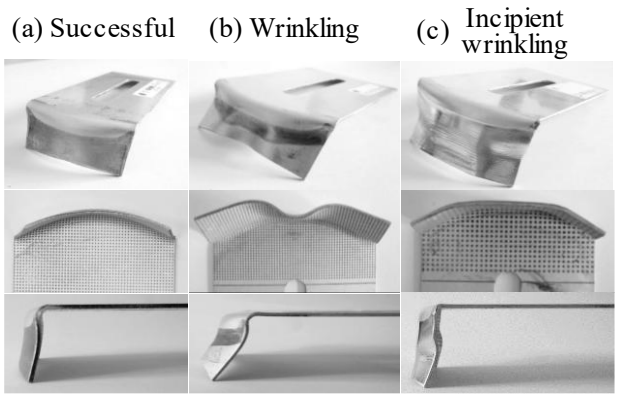

Figure 7. Three modes of failure observed in shrink flanging by SPIF: (a) Successful flange (S), (b) Flange with failure by wrinkling (W) and (c) flange failed by incipient wrinkling (IW).

Two modes of failure were observed: (1) Failure by wrinkling, labelled as 'W' and coloured in red, and (2) Failure by incipient wrinkling, labelled as 'IW' and coloured in yellow. The former refers to flanges that presented an edge clearly wrinkled after the forming operation, being useless flanges. The latter represent flanges that exhibited a polygonal edge that did not develop into an obvious wrinkle at the end of the forming process, so they are still functional flanges. This mode is named incipient wrinkling hereafter. Finally, the label S (successful) is used for flanges processed successfully (green colour). Figure 7 shows examples of a successful flange (a), a wrinkled flange (b) and a flange with incipient wrinkling (c) corresponding to the 45 mm radius die. The practical process window in each case is defined by the combination of parameters that yield successful flanges, that is, the green zone.

In view of Tables 3 and 4, it is pointed out that the results are substantially different depending on the die radius (R_{die}). Thus, flanges formed using $R_{die} = 45$ mm were susceptible to fail either by

wrinkling, 'W', or by incipient wrinkling, 'IW', whereas for $R_{die} = 20$ mm only incipient wrinkling was observed. Slight differences in formability were found varying ϕ_{tool}. For $R_{die} = 45$ mm, reducing the tool diameter from $\phi_{tool} = 20$ mm to $\phi_{tool} = 12$ mm produced a slight increase the formability, as can be observed in Table 3. This fact, commonly accepted in SPIF [41], was though not observed for $R_{die} = 20$ mm (see Table 4). On the other hand, no effect in terms of formability was observed in flanges processed either at $S = 20$ rpm or at $S = 1000$ rpm for both die radii.

Table 3. Experiments corresponding to R_{die} = 45 mm. S (Successful), W (failure by wrinkling) and IW (failure by incipient wrinkling).

Flange radius (R_{die}) of 45 mm							
Φ_{tool}	**S**	l_o	w_0 **[mm]**				
[mm]	**[rpm]**	**[mm]**	**36**	**45**	**54**	**63**	**72**
12	20	10				**S**	S
		15		S	S	**W**	W
		20	S	IW	**IW**		
		25	IW	IW			
	1000	10				S	S
		15	S	S	S	W	W
		20	S	IW	IW		
		25	IW	IW			
20	20	10			S	W	W
		15		S	W	W	W
		20	S	IW			
		25	IW	IW			
	1000	10			S	W	W
		15		S	W	W	W
		20	S	IW			
		25	IW	IW			

Table 4. Experiments corresponding to R_{die} = 20 mm. S (Successful), W (failure by wrinkling) and IW (failure by incipient wrinkling).

Flange radius (R_{die}) of 20 mm							
Φ_{tool}	**S**	l_o	w_0 **[mm]**				
[mm]	**[rpm]**	**[mm]**	**36**	**45**	**54**	**63**	**72**
12	20	15	S	S	**S**	**IW**	IW
		20	S	S	IW	IW	IW
		25					IW
	1000	15	S	S	S	IW	IW
		20	S	S	IW	IW	IW
		25					IW
20	20	15	S	S	S	IW	IW
		20	S	S	IW	IW	IW
		25					IW
	1000	15	S	S	S	IW	IW
		20	S	S	IW	IW	IW
		25					IW

According to the experimental results, it can be established that, for both dies radii analysed, a slightly higher formability was obtained using the forming tool of 12 mm diameter, regardless the spindle speed used. Generally speaking, it is pointed out that short and narrow flanges, i.e. flanges with both small l_0 and w_0, were successfully processed, whereas long and wide ones, i.e. flanges with large l_0 and w_0, failed systematically by wrinkling or incipient wrinkling. In the former case, the flanges are so narrow that their edges are not able to shrink enough to produce wrinkles, being the process similar to a conventional folding operation. In the latter one, the edge shrinkage is always high enough to produce wrinkling. In the intermediate range, the failure for each die radius is controlled by a combination of initial length and width of the flanges. Thus, for $R_{die} = 45$ mm, focusing for instance on Table 3 ($\phi_{tool} = 12$ mm and $S = 20$ rpm), flanges with w_0 below 54 mm and l_0 values up to 15 mm were successfully formed, and for w_0 above 54 mm the maximum l_0 allowed was 10 mm. In the case of $R_{die} = 20$ mm, see as reference Table 4 ($\phi_{tool} = 12$ mm and $S = 20$ rpm), flanges with w_0 below 24 mm were successfully formed for all the l_0 values tested, extending to 28 mm for l_0 up to 15 mm. These general rules establish the practical process window for the SPIFed flanges analysed in this study.

Finally, it is worth noticing that the maximum l_0/R ratio obtained for 45 mm die radius is ranging from 0.222 to 0.444 with w_0 varying from 20 to 72 mm, and for 20 mm die radius is ranging from 1 to 0.536 with w_0 varying from 20 to 28 mm. These values are compatible with the results obtained by Zhang et al. [26] for closed shrink flanges in AA5754-O sheets deformed by double-sided incremental forming as mentioned in the introduction. Furthermore, the l_0/R ratios achieved are above 10 times higher than the one obtained by Chen et al. [5] using rubber forming for this alloy. This highlights again the ability of the incremental deformation to improve the flangeability of the material.

6. Formability and wrinkling analysis.

In the following section a systematic analysis of the formability in terms of the winkle formation is presented. This includes: (i) the analysis of the formed flanges in the principal strain space, (ii) the assessment of the geometry of the flanges related to its mode of failure and (iv) the proposal of a methodology for wrinkling prediction in operations of shrink flanging by SPIF.

6.1. *Analysis in the principal strain space*

The analysis focused on some representative specimens highlighted in bold in Tables 3 and 4, including successful and failed flanges of each die radius formed with the 12 mm tool diameter at 20 rpm of spindle speed. These flanges represent the transition from the successful region to the failure region. The strain distribution of these flanges was evaluated experimentally using the Argus® system, following the methodology detailed in section 3. The strain results were also used to validate the FE model developed.

For the die radius $R_{die} = 45$ mm, the following flanges were analysed: (i) the successful flange of $w_0 = 63$ mm and $l_0 = 10$ mm, (ii) the flange of $w_0 = 63$ mm and $l_0 = 15$ mm failed by wrinkling and (iii) the one of $w_0 = 54$ mm and $l_0 = 20$ mm failed by incipient wrinkling.

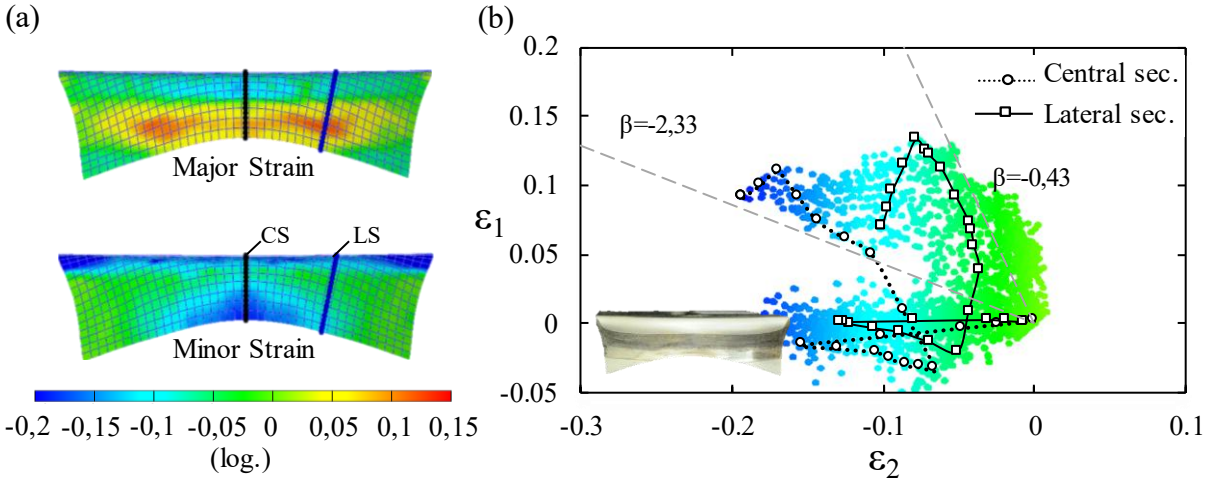

Figure 8. Successful flange for $R_{die} = 45$ mm: (a) Major and minor principal strain contours, and (b) principal strain map in the FLD showing the strain evolution along the central and the lateral sections (CS and LS). $w_0 = 63$, $l_0 = 10$ mm, $\phi_{tool} = 12$ mm and S=20 mm. Notice that the color scale in the FFD refer to the contour of minor strain.

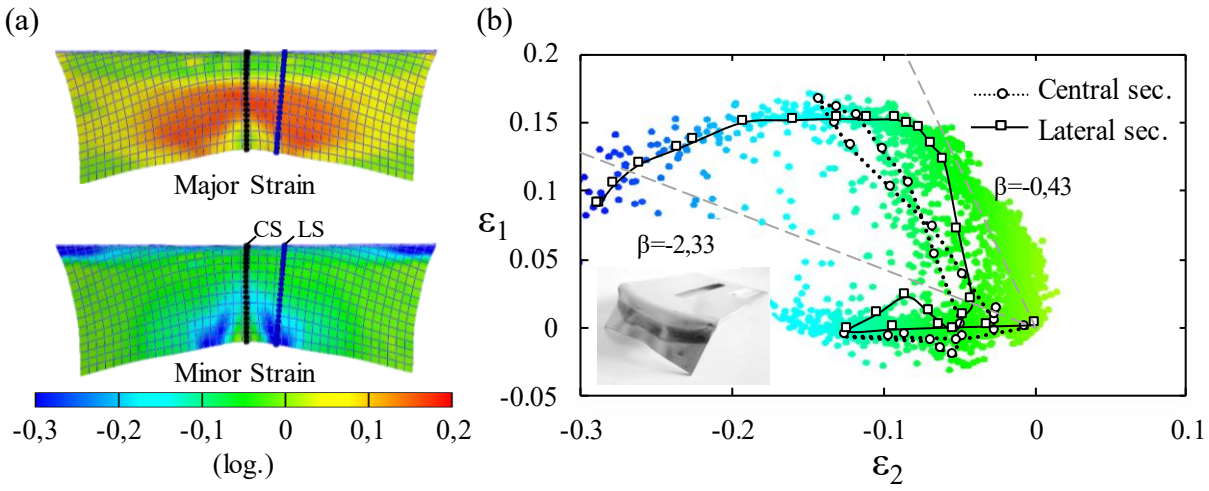

Figure 9. Flange failed by wrinkling for $R_{die} = 45$ mm: (a) Major and minor principal strain contours, and (b) principal strain map in the FLD showing the strain evolution along the central and the lateral sections (CS and LS). $w_0 = 63$, $l_0 = 15$ mm, $\phi_{tool} = 12$ mm and S=20 mm.

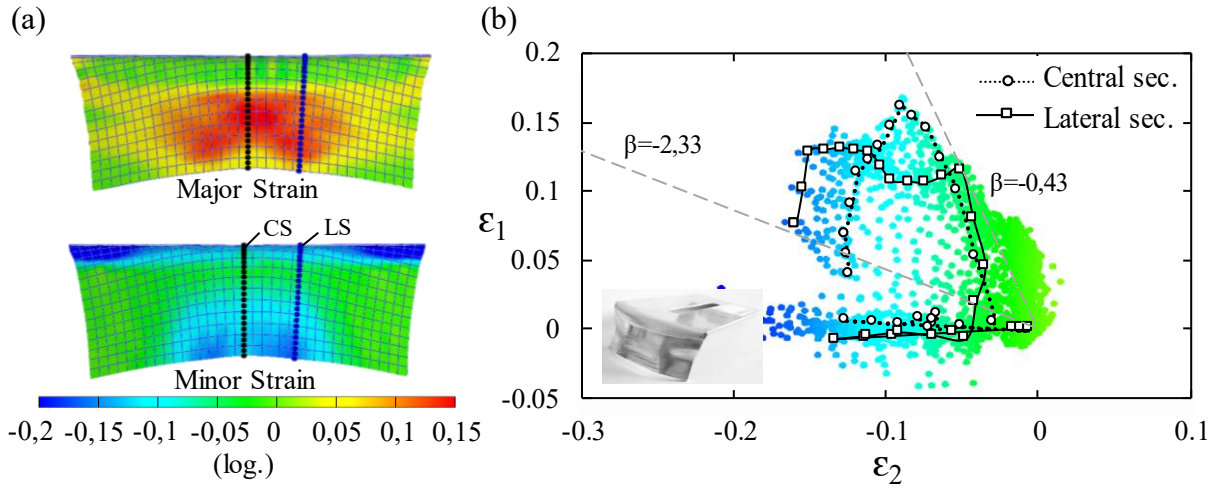

Figure 10. Flange failed by incipient wrinkling for $R_{die} = 45$ mm: (a) Major and minor principal strain contours, and (b) principal strain map in the FLD showing the strain evolution along the central and the lateral sections (CS and LS). $w_0 = 54$, $l_0 = 20$ mm, $\phi_{tool} = 12$ mm and S=20 mm.

Figures 8, 9 and 10 depict the principal strains in these specimens after forming. On the left-hand side (8a, 9a and 10a), the major and minor principal strain contours measured on the non-contact surfaces of each flange are shown. A picture of the contact surface is also provided. On the right-hand side (8b, 9b and 10b), the major and minor strains are represented in the FLD with the points coloured according to the minor strain values. The evolutions of the strain in two representative sections are also shown. The first one is the central section 'CS' (round dots), that is, the most compressed region at the flange wall, and therefore where wrinkles are most likely to begin. The second one, the lateral section 'LS' (square dots), is a section crossing the location of the highest value of major strain, located a few millimetres far from the central section. Both sections are indicated in black and blue

dots, respectively, in the strain colour maps on left-hand side (8a, 9a and 10a). In addition, to facilitate the analysis in the FLD, the strain paths for pure tension ($\beta = -0.43$) and pure compression ($\beta = -0.43$) obtained using the Barlat 89 plasticity criterion for the AA2024-T3 sheet are also depicted. As can be seen, either the central or lateral sections begin with a significant compression in the minor principal strain associated to the flange folding over the die. After that, the mayor strain increases up to reaching a maximum, ending in near pure compression state at the flange edge. It should be remembered that when using the Argus® system, the measured strains are limited to the inspected surface of the sheet (non-contact surface in this case) and that the physical sheet edge can neither be evaluated.

It is interesting to note that, in the successful flange (Figure 8), the last points measured near the edge flange in both sections present strain values above the line of pure compression ($\beta = -2.33$). In fact, all the points measured on the flange are clearly above this line, as shown in the figures. On the contrary, both the flange failed by wrinkling (Figure 9) and by incipient wrinkling (Figure 10) exhibit points well below the pure compression line. It should note that, in these flanges, wrinkles or incipient wrinkles are fully developed at the end of the forming process, so the strain values measured in the central or lateral section will depend on the wrinkle side inspected. That is, the concave face of the wrinkle offers smaller circumferential strains (minor principal strains) than in the case of the convex face. In particular, the lateral section in Figure 9 runs along the concave face of a wrinkle, whereas the central one does along a convex face. The same, although more attenuated, occurs in Figure 10. This will be better understood in the geometric analysis presented in the next section.

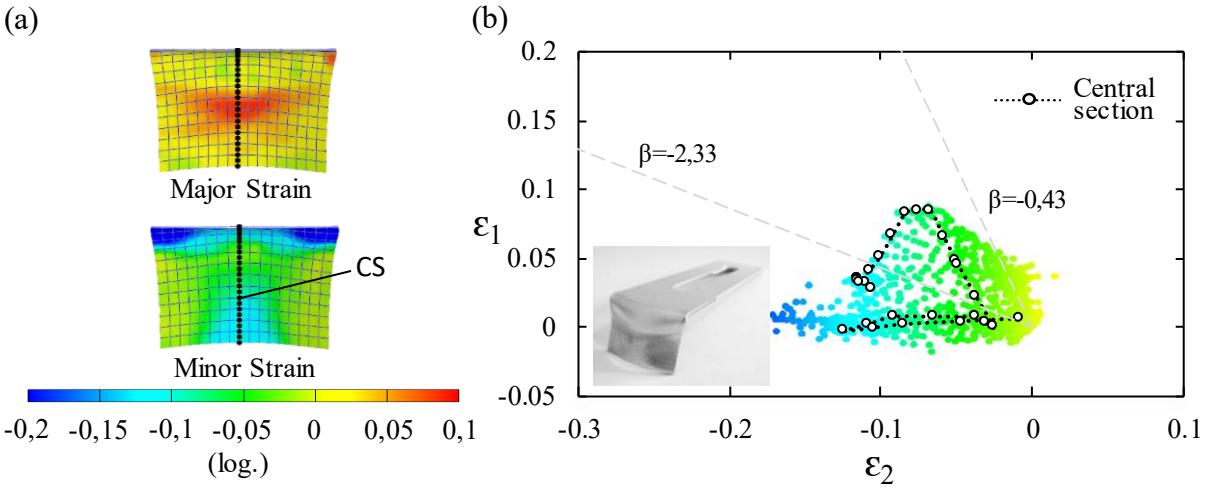

Figure 11. Successful flange for $R_{die} = 20$ mm: (a) Major and minor principal strain contours, and (b) principal strain map in the FLD showing the strain evolution along the central section (CS). $w_0 = 28$, $l_0 = 15$ mm, $\phi_{tool} = 12$ mm and S=20 mm.

A similar analysis was carried out for die radius $R_{die} = 20$ mm and the tests highlighted in bold in Table 4. They correspond to a successful flange of $w_0 = 28$ mm and $l_0 = 15$ mm (Figure 11) and a flange of $w_0 = 32$ mm and $l_0 = 15$ mm with incipient wrinkling (Figure 12). As can be seen in the contour map of principal strains (Figures 11a and 12a), the highest values of major and minor strain occur in the central section about the middle and at the edge of the flange respectively. For clarity only the central section is depicted in Figures 11b and 12b.

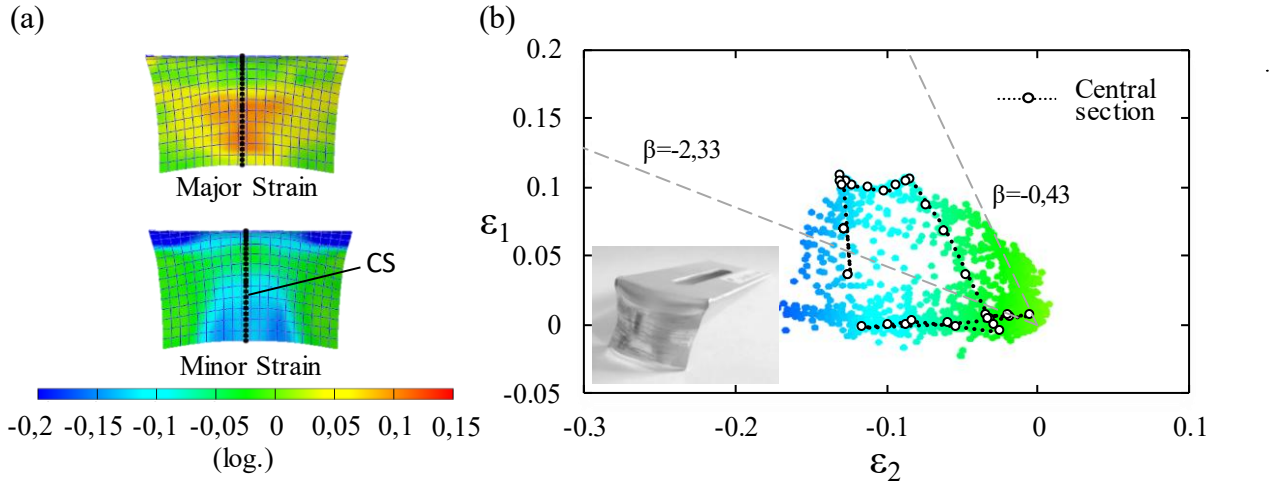

Figure 12. Flange failed by incipient wrinkling for $R_{die} = 20$ mm: (a) Major and minor principal strain contours, and (b) principal strain map in the FLD showing the strain evolution along the central section (CS). $w_0 = 32$, $l_0 = 15$ mm, $\phi_{tool} = 12$ mm and S=20 mm.

Focusing on the FLD (Figures 11b and 12b), two main differences with respect to the previous flanges are noticed. On the one hand, these flanges exhibit lower levels of major strains than the ones formed with $R_{die} = 45$ mm, indicating that they are exposed to a greater stretching during the flanging operation mainly due to the smaller die radius. On the other hand, either in the successful flange or the failed one, both present points at the flange edge well below the pure compression line. This points out that the pure compression line is not an effective wrinkling limit for incremental flanging in the FLD. As suggested in conventional processes [30, 31, 6], the wrinkling process in incremental forming should depend not only on the level of local strain/stress in the sheet but also on the specimen geometry, the material, and the test conditions. In this sense, the numerical model presented in section 4 will be used to analyse in depth the wrinkling phenomenon in shrink flanging by SPIF.

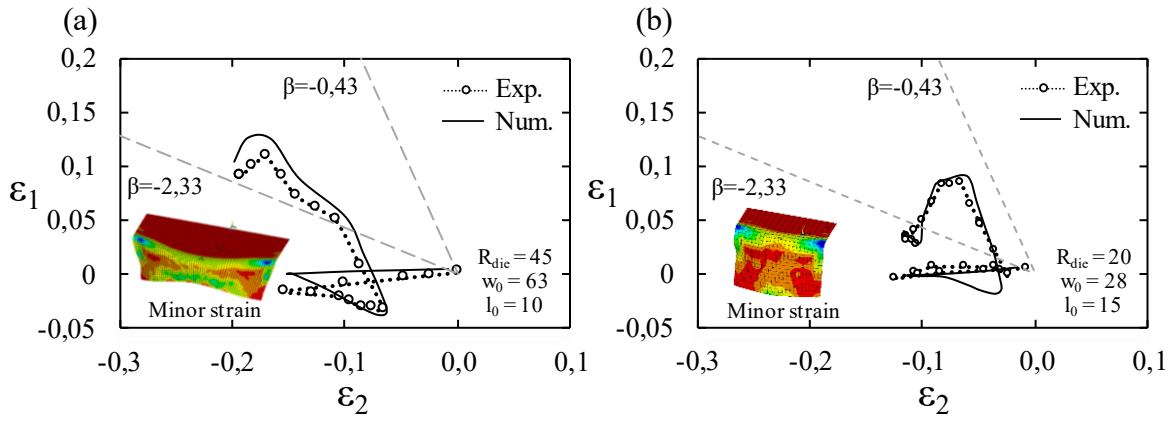

Figure 13. Experimental and numerical strains of the central section corresponding to successful flanges for (a) $R_{die} = 45$ mm and (b) $R_{die} = 20$ mm highlighted in Table 3 and Table 4 respectively.

In order to validate the FE model, Figure 13 shown the numerical versus experimental evolution of the major and minor principal strains along the central section of the successful flanges analysed in Figures 8 and 11, respectively. As can be seen, the numerical curves are in good agreement with their experimental counterpart, indicating a good accuracy of the FE model in terms of strains. Geometric accuracy is discussed in the next section.

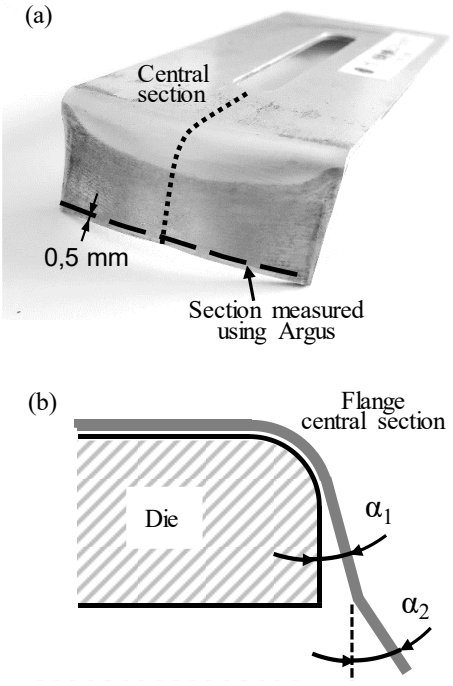

Figure 14. (a) Central and edge profiles considered in the geometric analysis. (b) Schematic springback angles measured at the root (α_1) and at the end (α_2) of the flange.

6.2. *Geometric analysis*

This section analyses the final geometry attained for the reference flanges presented in Figures 8 and 9 for $R_{die} = 45$ mm and Figures 11 and 12 for $R_{die} = 20$ mm. Two representative sections in the

final specimen were considered to (i) discuss the geometry deviations with respect to the desired shape and (ii) assess the capability of the FE model to predict the final shape of the flanges. These were the profile of the central section, depicted in Figure 14a, and the edge profile separated 0,5 mm from the tip of the flange, both obtained by the Argus® system.

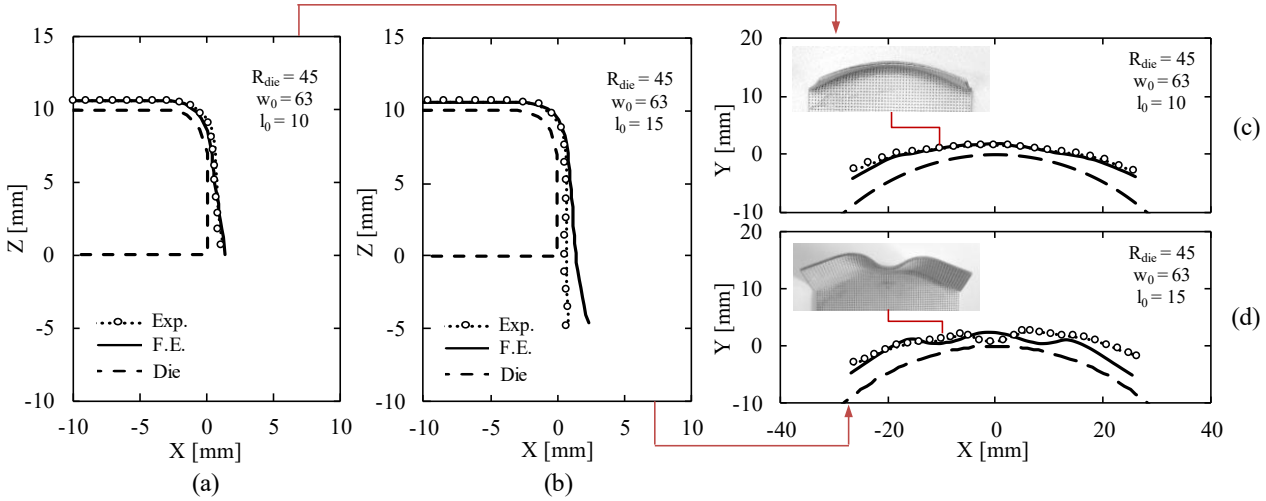

Figure 15. Experimental and numerical profiles for the successful (S) flange and the flange failed by wrinkling (W) highlighted, respectively, in Table 3 ($R_{die} = 45$ mm): (a) and (b) at the central section, and (c) and (d) at the edge of the flange. The die profile is depicted in dashed line.

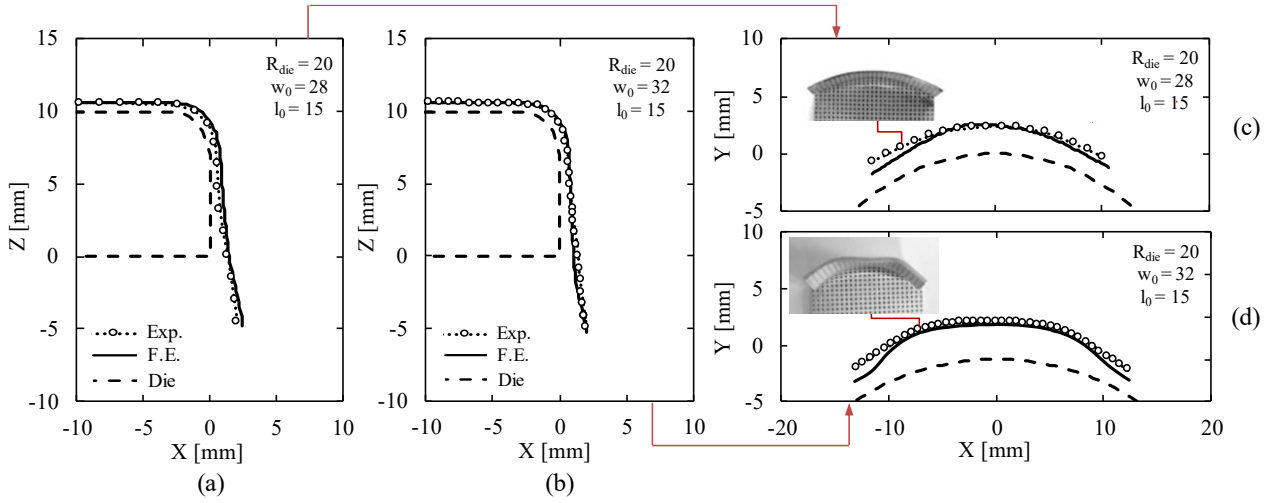

Figure 16. Experimental and numerical profiles for the successful (S) flange and the flange with incipient wrinkling (IW) highlighted, respectively, in Table 4 ($R_{die} = 20$ mm): (a) and (b) at the central section, and (c) and (d) at the edge of the flange. The die profile is depicted in dashed line.

Figure 15 and 16 show the profiles measured in the successful (S) flanges for 45 mm and 20 mm die radii, highlighted, respectively, in Table 3 and Table 4. The central profiles are depicted in (a), and the edge profiles are in (c). The die profile is also depicted in dashed line.
A noticeable springback was observed in both flanges. For the large die ($R_{die} = 45$ mm), the central edge had a recovery angle of 3º at the root of the flange, which increased to 7.2º at its end (see schema in Figure 14b). The edge profile showed a slighted increase of the final flange radius. Similar behaviour was observed in the small die ($R_{die} = 20$ mm). In this case, the central edge showed a recovery angle of 3.8º at the base and 5.4º at the end of flange. In contrast, the edge profile seemed to retain the final radius of the die much better. The numerical profiles obtained from the FE model are also shown in Figure 15 and 16. As can be seen, there was a good agreement with the experimental profiles in both the central and the edge sections.

Figure 15 and 16 depicts the experimental and numerical profiles in the flange failed by wrinkling and incipient wrinkling in Table 3 ($R_{die} = 45$ mm) and Table 4 ($R_{die} = 20$ mm), respectively. The central profiles are depicted in (b), and the edge profiles are in (d). As expected, there were a sizeable mismatch between the desirable and the actual shape due to both the wrinkling progression and the elastic recovery. For 45 mm of die radius (Figure 15), the numerical simulation was able to capture the initiation and development of the wrinkles. Although, they appeared toward the opposite side of the experimental ones. This numerical fact, usual when modelling unstable processes such as wrinkling by local buckling, is not relevant for our purposes since the aim was predicting the instant of the appearance of wrinkles and not their development. For the flange of 20mm die radius (Figure 16), the numerical and experimental profiles are again in good agreement, reproducing successfully the springback and the polygonization of the flange edge.

In summary, the analysis carried out indicates that elastic recovery is a factor of primary importance in shrink flanging by single-stage SPIF. The final geometric precision of the flange may be improved by designing different forming strategies other than the single pass scheme analysed in this work. Thus, forming strategies that include over-bending and/or multiple passes may greatly reduce the springback of the flange. This analysis is though beyond the aim of the present work.

Finally, the FE model has been shown as an effective tool to reproduce the final shape in successful flanges and flanges with incipient wrinkling. In wrinkled flanges, although it does not always ensure the direction of the wrinkles, which is highly affected by local flaws in the sheet, it is a useful tool for predicting the onset of wrinkling.

6.3. *Wrinkling prediction*

The appearance of wrinkles is the result of an unstable local buckling process caused by compressive stresses in the plane of the sheet. The following section aims to develop a general methodology to determine the critical stress conditions that activate the onset of wrinkling in incremental flanging processes as those analysed in this work.

The following two-steps approach is carried out: (1) Establishing the onset of wrinkling in failed specimens, and (2) determining the stress conditions that trigger the wrinkling process (critical or limit stress of winkling).

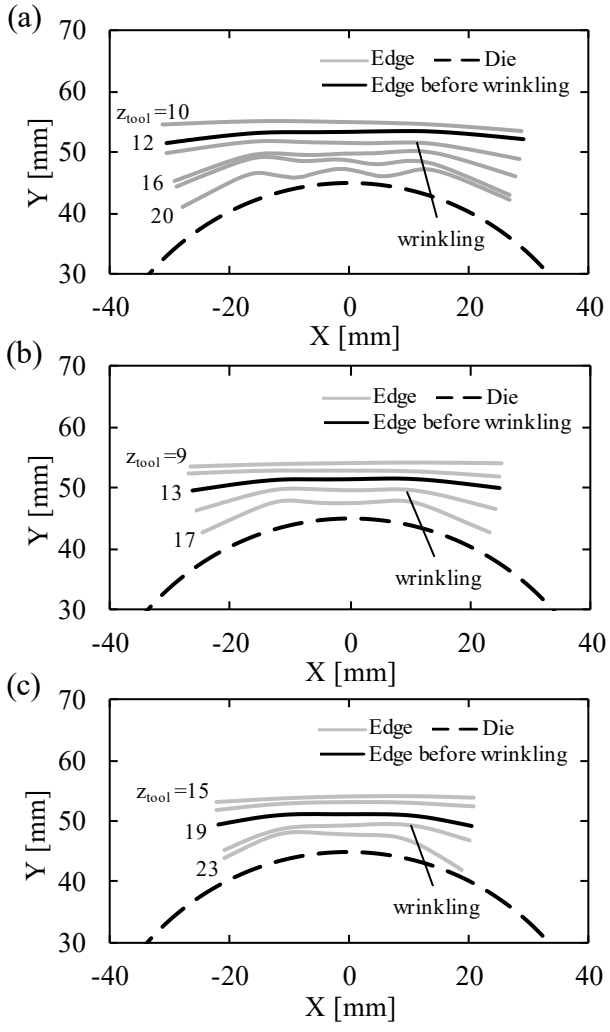

Figure 17. Numerical edge profile evolution at different stages of the forming process for $R_{die} = 45$ mm corresponding to (a) the flange failed by wrinkling of $w_0 = 63$ mm and $l_0 = 15$ mm, (b) and (c) the flanges failed by incipient wrinkling of $w_0 = 54$ mm and $l_0 = 20$ mm (b) and $w_0 = 45$ mm and $l_0 = 20$ mm, respectively.

Focusing on the incremental flanging for 45 mm in die radius, Figure 17 shows the numerical evolution of the edge profile of a series of failed flanges at several stages in the forming process, represented by the position in depth of the forming tool (z_{tool}) with respect to the original position of the blank surface. The flanges depicted are: one failed by wrinkling, Figure 17a ($w_0 = 63$ mm, $l_0 = 15$ mm), and two failed by incipient wrinkling, Figure 17 b ($w_0 = 54$ mm, $l_0 = 20$ mm) and Figure 17c ($w_0 = 63$ mm, $l_0 = 15$ mm) respectively.

The onset of wrinkling is defined as the instant (tool depth) at which the flange profile deviates from a convex shape to show a polygonal profile. Notice that this definition does not conflict with the distinction between failure by wrinkling or by incipient wrinkling proposed in section 5, that analysed exclusively the flange edge profile at the end of the process.

As can be seen in Figure 17a, the onset of wrinkling for that flange begins at value of z_{tool} between 12 mm and 14 mm. A critical tool depth (z^{crit}) of 12 mm is selected as last instant before triggering wrinkles (highlighted in bold) for this flange. In a similar way, a z^{crit} of 13 mm and 19 mm are observed for flanges in Figures 17b and 17c, respectively.

The critical stress of winkling (σ_{crit}) in the incremental process is defined as the in-plane compressive stress at the onset of wrinkling at the central point of the flange edge. As seen in section 6.1, the central point of the edge is the most compressed location of the flange and, therefore, where wrinkles are most likely to initiate.

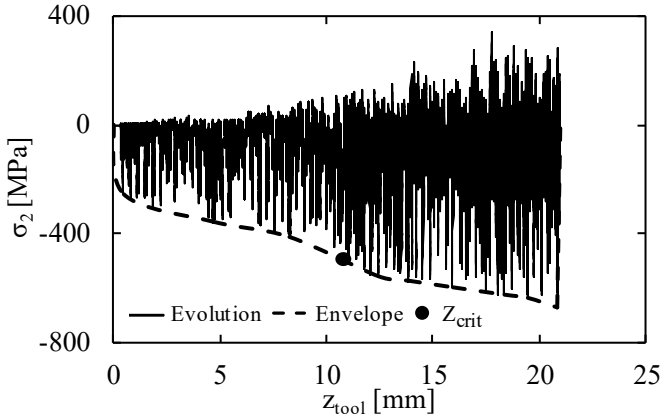

Figure 18. In-plane minor principal stress (σ_2) of the central point at the edge of the flange versus tool depth (z_{tool}) corresponding to the successful flange of $w_0 = 63$ mm and $l_0 = 15$ mm for $R_{die} = 45$ mm.

Figure 18 shows the in-plane minor principal stress evolution (σ_2) versus z_{tool} at the central point of the edge for the flange in Figure 17a. The typical cyclic pattern due to the incremental deformation process is evidenced. In addition, the envelope of local minima of σ_2 is depicted in dashed line. According to the definition above, the critical stress of winkling (σ_{crit}) corresponds to the value of σ_2 at the z^{crit} previously estimated in 12 mm, giving a value about -530 MPa. This process was repeated for the other two flanges.

Figure 19a depicts the σ_2 envelopes for the three flanges analysed, showing the critical stress of winkling corresponding to each case. As can be seen, these values are very similar, which is not surprising considering that the die radius, material, and test conditions remain constant. The average critical stress of wrinkling for $R_{die} = 45$ mm is about $\sigma_{crit} = -530$ MPa. This value represents an estimation of the wrinkling limit in term of stress for this flanging process. This means that any other tests with an evolution of σ_2 below this limit should initiate wrinkling at some point of the edge. In contrast, any test with a level of σ_2 above this limit should yield successful flanges.

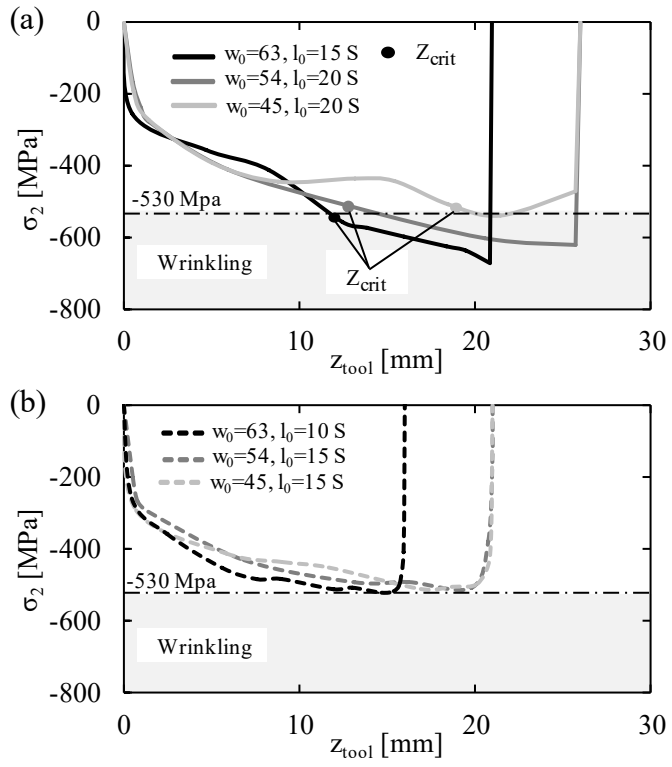

Figure 19. Evolution of the σ_2 envelopes of the central point at the edge of the flange versus tool depth (z_{tool}). (a) Three flanges with wrinkles presented in Figure 17. (b) Three successful flanges for $R_{die} = 45$ mm near the boundary of failure. The average critical stress of wrinkling for $R_{die} = 45$ mm is shown in dashed line ($\sigma_{crit} = -530$ MPa).

To verify this assumption, three successful tests were numerically simulated. These are the tests for $w_0 = 63$ mm - $l_0 = 10$ mm, $w_0 = 54$ mm - $l_0 = 15$ mm, and $w_0 = 45$ mm - $l_0 = 15$ mm corresponding to successful flanges near the boundary of failure (see Table 3). Figure 19b shows the evolution of the σ_2 envelopes for these three flanges. As expected, all of them are slightly above the level of $\sigma_{crit} = -530$ MPa, without intersecting this limit during the forming process.

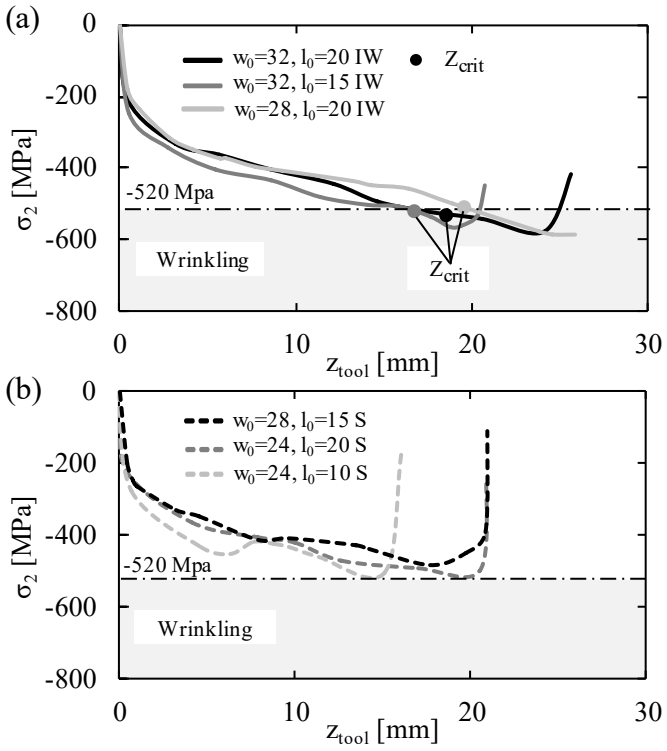

Figure 20. Evolution of the σ_2 envelopes of the central point at the edge of the flange versus tool depth (z_{tool}). (a) Three flanges with wrinkles for $R_{die} = 20$ mm. (b) Three successful flanges near the boundary of failure. The average critical stress of wrinkling for $R_{die} = 20$ mm is shown in dashed line ($\sigma_{crit} = -520$ MPa).

Following the same methodology, the critical stress for wrinkling for the incremental flanging over $R_{die} = 20$ mm was estimated. Figure 20a shows the σ_2 envelopes of the three failed flanged analyzed. Again, the critical stresses were very similar, having an average value of $\sigma_{crit} = -520$ MPa. This value, although close, is different for the one obtained for $R_{die} = 45$ mm, pointing out the influence of the die radius on the wrinkling limit. However, it also shows that this influence is considerably less than that observed in the conventional shrink flanging process. Figure 20b depicts the evolution of three successful flanges for $R_{die} = 20$ mm near the boundary of failure (see Table 4). As before, they evolve above the wrinkling limit of $\sigma_{crit} = -520$ MPa, corroborating again the proposed methodology for wrinkling prediction.

6. Conclusions

This work presents a critical experimental and numerical study of the shrink flanging process by SPIF of AA2024-T3 sheets. Two die radii of 45 mm and 20 mm and different process conditions were investigated to establish the process window, failure modes and geometric capability of this incremental flanging operation. The following conclusions have been drawn:

- The limiting event of sheet formability was the wrinkling formation by two modes of failure: (1) failure by wrinkling, referring to flanges with obvious wrinkles by local buckling, and (2) failure by incipient wrinkling, referring to flanges exhibiting a polygonal edge but without developing wrinkles. The former are clearly useless flanges whereas the latter are still functional.
- The failure by wrinkling was observed for $R_{die} = 45$ mm of large initial width, typically w_0 above 54 mm. Failure by incipient wrinkling predominated for short width as the initial length increased, being also the unique mode of failure observed for $R_{die} = 45$ mm.
- Reducing the tool diameter enhances notably the formability for $R_{die} = 45$ mm, whereas it did not cause any effect on the process for $R_{die} = 20$ mm. An increase in spindle speed from did not produce appreciable effects on formability in any of the flanges tested.
- The analysis in the principal strain space pointed out that the pure compression line is not an effective wrinkling limit curve for incremental flanging in the FLD. In both successful and failed flanges for both die radii, it was observed that the points on the edge of the flange were located indistinctly above and below this line.
- The geometric analysis revealed that the shrink flanging process by single-stage SPIF induces a significant springback in the final part. Different forming strategies, involving over-bending and/or multiple passes, are needed to reduce this geometric deviation.
- A numerical methodology to predict the onset of wrinkling in incremental flanging processes is presented. This establishes the winkling limit as the value of in-plane minor (compressive) stress of the central point at the edge of the flange (limit stress of winkling) that trigger the wrinkling process. Thus, for a given test, a successful flange is predicted when the minor stress at this point is always above the critical stress during the forming process.
- A wrinkling limit of -530 MPa and -520 MPa was obtained for 45 mm and 20 mm die radius flanges respectively, leading to predictions in very good agreement with the experimental results in AA2024-T3 sheets.

References

[1] https://www.sonexaircraft.com/eshop/cart.php?target=product&product_id=16449. Last accessed on 10 January 2022.

[2] Dudra S. and Shah S. Stretch flanges: Formability and trimline development, Journal of Material Shaping Technology Vol. 6 (1988), pp. 91–101. https://doi.org/10.1007/BF02834824.

[3] Nader Asnafi. On stretch and shrink flanging of sheet aluminium by fluid forming, Journal of Materials Processing Technology Vol. 96 (1999), pp. 198-214. https://doi.org/10.1016/S0924-0136(99)00352-0.

[4] Livatyali H, Muderrisoglu A, Ahmetoglu M, Akgerman N, Kinzel G and Altan T. Improvement of hem quality by optimizing flanging and pre-hemming operations using computer aided die design. J Mater Proc. Tech. Vol. 98 (2000), pp. 41–52. https://doi.org/10.1016/S0924-0136(99)00304-0.

[5] Chen L, Chen H, Wang Q, Li Z. Studies on wrinkling and control method in rubber forming using aluminium sheet shrink flanging process. Materials and Design, Vol. 65 (2015), pp. 505-510. https://doi.org/10.1016/j.matdes.2014.09.057.

[6] Wang X, Cao J, Li M. Wrinkling analysis in shrink flanging. ASME J Manuf Sci Eng Vol. 223(3) (2001), pp. 426-432. https://doi.org/10.1115/1.1381397.

[7] Chen L., Bai Y., Jiang Z., Chen H., Wu C. and Wang Q. Numerical and experimental studies on wrinkling control methods of sheet metal part with high curvature and large flange in rubber forming. Advanced in Mechanical Engineering, vol. 11(10) (2019), pp. 1-8. DOI: 10.1177/1687814019883787

[8] Emmens WC, Sebastiani G., Van den Boogaard AH. The technology of incremental sheet forming - A brief review of the history. Journal of Materials Processing Technology, Vol. 210(8) (2010), pp. 981-997. https://doi.org/10.1016/j.jmatprotec.2010.02.014.

[9] J. Jeswiet, F. Micari, G. Hirt, A. Bramley, J. Duflou, J. Allwood, Asymmetric Single Point Incremental Forming of Sheet Metal, CIRP Annals, Vol. 54(2) (2005), pp. 88-114. https://doi.org/10.1016/S0007-8506(07)60021-3.

[10] Emmens WC, Van den Boogaard AH. An overview of stabilizing deformation mechanisms in incremental sheet forming. Journal of Material Processing Technology, Vol. 209(8) (2009), pp. 3688-3695. https://doi.org/10.1016/j.jmatprotec.2008.10.003.

[11] Gatea S, Ou H, McCartney G. Review on the influence of process parameters in incremental sheet forming. The International Journal of Advanced Manufacturing Technology, Vol 87(1-4) (2016), pp. 479-499. https://doi.org/10.1007/s00170-016-8426-6.

[12] Cui Z, Gao L. Studies on hole-flanging process using multistage incremental forming, CIRP Journal of Manufacturing Science and Technology, Vol. 2(2) (2010), pp. 124-128. https://doi.org/10.1016/j.cirpj.2010.02.001.

[13] Movahedinia H, Mirnia M J, Elyasi M and Baseri H. An investigation on flaring process of thin-walled tubes using multistage single point incremental forming. International Journal of Advanced Manufacturing Technology Vol. 94 (2018), pp. 867-880. https://doi.org/10.1007/s00170-017-0971-0

[14] Allwood JM, Shouler DR. Paddle forming: a novel class of sheet metal forming processes. Annals of the CIRP vol. 56/1/2007, pp. 257-260. https://doi.org/10.1016/j.cirp.2007.05.060

[15] Besong L.I., Buhl J. and Bambach M. Investigations on hole-flanging by paddle forming and a comparison with single point incremental forming. International Journal of Mechanical Sciences, vol. 164 (2019) 1051 43. https://doi.org/10.1016/j.ijmecsci.2019.105143

[16] Chen X., Wen T., Hu J., Zhang M. and Fang J. Investigation of factors affecting the formability of metallic sheets in dieless incremental hole-flanging. The International Journal of Advanced Manufacturing Technology, vol. 103 (2019) pp. 2609–2620. https://doi.org/10.1007/s00170-019-03459-x

[17] Wen T., Zhang S., Zheng J., Huang Q. and Liu Q.. Bi-directional dieless incremental flanging of sheet metals using a bar tool with tapered shoulders. Journal of Materials Processing Technology, vol. 229 (2016) pp. 795-803. http://dx.doi.org/10.1016/j.jmatprotec.2015.11.005.

[18] Centeno G, Silva MB, Cristino VAM, Vallellano C, Martins PAF. Hole-flanging by incremental sheet forming. International Journal of Machine Tools and Manufacture, Vol. 59 (2012), pp. 46-54. https://doi.org/10.1016/j.ijmachtools.2012.03.007.

[19] Cristino V.A., Montanari L., Silva M.B., Atkins A.G. and Martins P.A.F. Fracture in hole-flanging produced by single point incremental forming. International Journal of Mechanical Sciences, vol. 83 (2014), pp. 146-154. http://dx.doi.org/10.1016/j.ijmecsci.2014.04.001.

[20] Martínez-Donaire AJ, Borrego M, Morales-Palma D, Centeno G, Vallellano C. Analysis of the influence of stress triaxiality on formability of hole-flanging by single-stage SPIF, International Journal of Mechanical Sciences, Vol. 151 (2019), pp. 76-84. http://dx.doi.org/10.1016/j.ijmecsci.2018.11.006.

[21] Seyyedi S.E. Gorji H., Mirnia M.J., and Bakhshi-Jooybari M.. Prediction of ductile damage and fracture in the single- and multi-stage incremental hole-flanging processes using a new damage accumulation law. The International Journal of Advanced Manufacturing Technology, vol. (2022) 119, pp. 4757–4780. https://doi.org/10.1007/s00170-021-08638-3.

[22] Borrego M, Morales-Palma D, Martinez-Donaire A, Vallellano C. (2016) Experimental study of hole-flanging by single-stage incremental sheet forming. Journal of Material Processing Technology Vol. 237, pp. 320-330. https://doi.org/10.1016/j.jmatprotec.2016.06.026.

[23] Morales-Palma D, Borrego M, Martínez-Donaire A. J., Centeno G and Vallellano C. Optimization of Hole-Flanging by Single Point Incremental Forming in Two Stages, Materials, 2018, vol. 11(10), 2029. https://dx.doi.org/10.3390%2Fma11102029.

[24] Voswinckel H, Bambach M, Hirt G. Process limits of stretch and shrink flanging by incremental sheet metal forming. Key Engineering Materials, Vol. 549 (2013), pp. 45–52. http://dx.doi.org/10.4028/www.scientific.net/KEM.549.45.

[25] Voswinckel H, Bambach M, Hirt G. Improving geometrical accuracy for flanging by incremental sheet metal forming. International Journal of Material Forming, Vol. 8(5) (2015), pp. 391-399. https://doi.org/10.1007/s12289-014-1182-y.

[26] Zhang H, Zhang Z, Ren H, Cao J, Chen J. Deformation mechanics and failure mode in stretch and shrink flanging by double-sided incremental forming. International Journal of Mechanical Sciences Vol. 144 (2018), pp. 216-222. https://doi.org/10.1016/j.ijmecsci.2018.06.002.

[27] Lopez-Fernandez J, Centeno G, Martinez-Donaire A, Morales-Palma D, Vallellano C. Stretch-flanging of AA2024-T3 sheet by single-stage SPIF. Thin-Walled Structures Vol. 160:107338 (2021). https://doi.org/10.1016/j.tws.2020.107338.

[28] Martins PAF, Bay N, Tekkaya AE, Atkins AG. Characterization of fracture loci in metal forming. International Journal of Mechanical Sciences, Vol. 83 (2014), pp. 112-123. https://doi.org/10.1016/j.ijmecsci.2014.04.003.

[29] Havranek J. Wrinkling limit of tapered pressing. J Aust Inst Met, Vol. 20 (1975), pp. 114–119.

[30] A.M. Szacinski, P.F. Thomson. Investigation of the existence of a wrinkling-limit curve in plastically-deforming metal sheet, J Mater Process Technol, Vol. 25(2) (1991), pp. 125-137.

[31] Narayanasamy, R. Sowerby. Wrinkling of sheet metals when drawing through a conical die, Journal of Materials Processing Technology, Vol. 41(3) (1994), pp. 275-290.

[32] Magrinho J, Silva C, Silva MB, Martins PA. Formability limits by wrinkling in sheet metal forming. Proceedings of the Institution of Mechanical Engineers, Part L: Journal of Materials: Design and Applications, Vol. 232(8) (2018) pp. 681-692. https://doi.org/10.1177%2F1464420716642794.

[33] Sebastian Härtel, Birgit Awiszus, New Processing Technologies of Incremental Sheet Metal Forming, Procedia Engineering, Vol. 81 (2014), pp. 2311-2317. https://doi.org/10.1016/j.proeng.2014.10.326.

[34] S.W. Chen, M. Zhan, P.F. Gao, F. Ma, H.R. Zhang. A new robust theoretical prediction model for flange wrinkling in conventional spinning, Journal of Materials Processing Technology, Vol. 288 (2021), 116849. https://doi.org/10.1016/j.jmatprotec.2020.116849.

[35] ASTM Standard E8/E8M – 09. Standard tests methods for tension testing of metallic materials, 2009.

[36] ASTM Standard E 517 – 00. Standard method for plastic strain ratio r for sheet metal, 2000.

[37] International Standard ISO 12004-2:2008. Metallic materials-sheet and strip determination of forming limit curves, Part 2: Determination of forming limit curves in the laboratory, 2008.

[38] Martínez-Donaire AJ, García-Lomas FJ, Vallellano C. New approaches to detect the onset of localised necking in sheets under through-thickness strain gradients, Materials and Design, Vol. 57 (2014), pp. 135-145. https://doi.org/10.1016/j.matdes.2014.01.012.

[39] Vallellano C, Morales D, Lomas-Jung FJ. A study to predict failure in biaxially stretched sheets of aluminum alloy 2024-T3. Materials and Manufacturing Processes Vol. 23(3) (2008), pp. 303-310. https://doi.org/10.1080/10426910801974804.

[40] Centeno G, Doblas FJ, Martínez-Palmeth LH, Martínez-Donaire AJ, Vallellano C. FEA of the bending effect in the formability of metal sheets via incremental forming, Steel Research International, Spl. Issue Metal Forming 2012, pp. 447-450.

[41] Silva, M., Teixeira, P., Reis, A., Martins, P. On the formability of hole-flanging by incremental sheet forming. Proceedings of the Institution of Mechanical Engineers, Part L: Journal of Materials: Design and Applications, Vol. 227(2) (2013), pp. 91-99. https://doi.org/10.1177%2F1464420712474210.

[42] Silva MB, Skjoedt M, Atkins AG, Bay N, Martins PAF. Single–point incremental forming and formability–failure diagrams. J Strain Anal Eng Des Vol. 43(1) (2008) pp. 15-31. http://dx.doi.org/10.1243/03093247JSA340.

[43] Skjoedt M, Silva MB, Martins PAF and Bay N. Strategies and limits in multi-stage single-point incremental forming. J. Strain Anal Eng. Des. Vol. 45 (2010), pp. 33–44. https://doi.org/10.1243%2F03093247JSA574.

[44] Barlat F, Lian J. Plastic behaviour and stretchability of sheet metals. part i: A yield function for orthotropic sheets under plane stress conditions. Int Journal of Plasticity Vol. 5(1) (1989), pp. 51-66. https://doi.org/10.1016/0749-6419(89)90019-3.

[45] Logan R and Hosford W Upper-bound anisotropic yield locus calculations assuming (111)-pencil glide. International Journal of Mechanical Sciences Vol. 22 (1980), pp. 419-430. https://doi.org/10.1016/0020-7403(80)90011-9.

[46] Benedetti M, Fontanari V, Monelli B, Tassan M. Single-point incremental forming of sheet metals: Experimental study and numerical simulation. Proceedings of the Institution of Mechanical Engineers, Part B: Journal of Engineering Manufacture. Vol. 231(2) (2017), pp. 301-312. https://doi.org/10.1177/0954405415612351.

[47] Zhang M H, Lu B, Chen J, Long H and Ou H. Selective element fission approach for fast FEM simulation of incremental sheet forming based on dual-mesh system. International Journal of Advanced Manufacturing Technology, Vol. 78 (2015), pp. 1147-1160. https://doi.org/10.1007/s00170-014-6723-5.